

# Efficient simulation of EUV multilayer defects with rigorous data base approach

P. Evanschitzky, F. Shao<sup>\*</sup>, A. Erdmann

Fraunhofer Institute for Integrated Systems and Device Technology  
Schottkystrasse 10, 91058 Erlangen, Germany  
<sup>\*</sup>now with Mentor Graphics, China

## ABSTRACT

This paper presents the extension of the well-established rigorous electromagnetic field (EMF) solver Waveguide for the efficient and fully rigorous simulation of patterned extreme ultraviolet (EUV) masks with multilayer defects using a rigorously computed multilayer defect data base combined with on demand computed absorber structures. Typical computation times are in the range of seconds up to a few minutes. The new simulation approach will be presented. Selected simulation examples and a defect repair example demonstrate the functionality and the capability to perform fast, highly accurate and flexible EUV multilayer defect computations.

**Keywords:** Lithography simulation, EUV multilayer defects, rigorous EMF simulation, multilayer defect data base

## 1. INTRODUCTION

Defects below and inside multilayers of EUV masks belong to the most critical concerns for the application of EUV lithography in manufacturing processes. These defects are difficult to inspect and to repair. Moreover, they may print at different focus positions. Therefore, systematic investigations and classifications of such defects and the development of defect repair strategies are essential. This work can only be performed with the help of simulations. In order to deal with the very specific and challenging simulation task, different approaches based on fully rigorous EMF solvers, partially rigorous EMF solvers and analytical approximation models have been presented. However, due to the high sensitivity of the simulation results to the defect parameters, the large defect parameter range, the complex structure of defective multilayers and the required accuracy the application of a fully rigorous EMF solver seems to be indispensable. One of the biggest challenges to be solved is the extensively long simulation time for the rigorous computation of EUV multilayer defects.

A solution of this problem is the extension of the well-established rigorous EMF solver Waveguide [1] (comparable to RCWA) with a defect data base for the efficient simulation of patterned EUV masks with multilayer defects. A typical and fully rigorous EUV multilayer defect simulation with our Waveguide solver takes several hours on a state of the art personal computer. This includes already extensive optimizations of all parts of the simulation algorithm. Such long simulation times make the systematic defect investigation and in particular the defect repair investigation very difficult. A powerful solution of the problem with the important feature to keep the fully rigorous simulation is a defect data base approach. The idea of this approach is to split-up the mask into the defective multilayer part and the absorber part. Both parts are computed rigorously using the Waveguide solver. The time consuming computations of the defective multilayer part can be performed separately and continuously for numerous systematically varied defect parameters and the results will be stored in a data base. Since the simulation time of the absorber part is usually in the range of seconds this part will be computed on demand during an investigation. This ensures the flexibility required for defect repair simulations. The coupling of the flexible on demand absorber simulation with the defect data base leads to very fast simulations with a large parameter range. The computation time of such a coupled and fully rigorous simulation of a patterned EUV mask with multilayer defect is in the range of seconds up to a few minutes.

In Section 2 the new simulation approach will be presented. In Section 3 the accuracy and speed of the new approach with respect to fully rigorous simulations without data base are investigate in detail. Finally, the simulation example of a

defect repair demonstrates the functionality and the capability to perform fast, highly accurate and flexible EUV multilayer defect computations.

## 2. SIMULATION MODEL

### 2.1. Waveguide approach

The basic idea of the computation of light diffraction from a lithography mask with the Waveguide method can be derived from Figure 1 left.

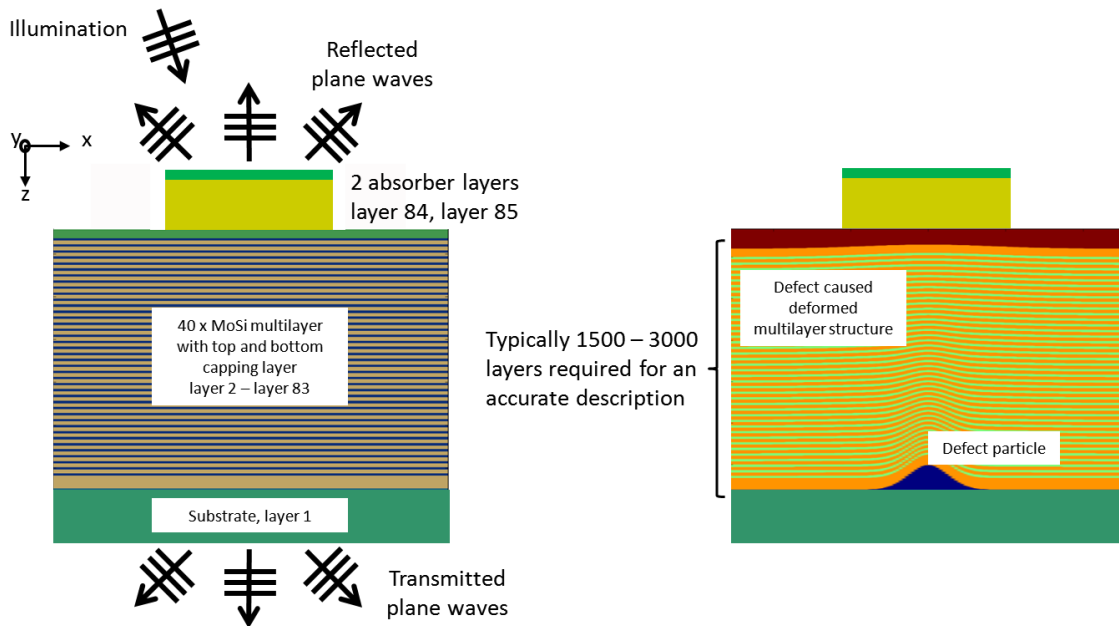


Figure 1: Left: Defect free EUV mask with oblique illumination and resulting transmitted and reflected diffraction spectrum. Right: EUV mask with defect onto the substrate and defect caused deformation of the whole multilayer structure. In contrast to the defect free mask several thousand layers have to be used for an accurate description of the geometry.

Based on the real mask geometry a slicing of the area to be simulated is performed by defining maximum sized layers which are homogeneous in the direction of light propagation (see layer 1 – layer 85 in Figure 1 left). This is the so called Waveguide assumption. Depending on the layout and on the required resolution the geometry (material distribution) inside the individual layers is described by an arbitrary number of rectangles with arbitrary sizes. Using such a mask description any geometry can be realized and a potential sampling error can be limited to the desired value. In particular the very typical Manhattan like structures can be described fully correct without any sampling error. In the next step the material distributions and the electromagnetic fields of all layers are expressed by Fourier series. All Fourier series are truncated according to the number  $M$  of modes which are supposed to be taken into account. In Figure 1 left exemplarily three reflected and three transmitted diffraction orders (modes) are shown. The combination of this material and field descriptions with the Maxwell equations leads to an eigenvalue problem for each layer and finally to the propagating and evanescent modes inside the layers. By applying the appropriate boundary conditions all layers are coupled and the resulting reflected and transmitted plane waves at the top and bottom side of the mask are computed (see Figure 1 left). Because of the periodic boundary conditions in lateral direction ( $xy$ -plane, perpendicular to the direction of light propagation), the mask is always regarded as a periodic structure. Isolated features can be simulated by using a mask period which is large enough for the respective problem. The integration of other boundary conditions like the perfectly matched layers (PML) boundaries [2] is currently under investigation. Two dimensional (e.g. lines) and three

dimensional (e.g. contact holes) computations are possible with the method. A detailed mathematical description of the Waveguide method including simulation examples and further information on modal methods can be found in [1, 3 - 5].

The computation time is proportional to  $A \cdot M^3$ .  $A$  is the number of layers consisting of more than one material after the described mask slicing.  $M$  is the overall number of modes used for the computation and can be expressed by  $M = (2N_x + 1) \cdot (2N_y + 1)$ . According to all investigations performed so far the following size is required for  $N_{x,y}$ :  $N_{x,y} = b_{x,y}/2\lambda$  for EUV masks and  $N_{x,y} = 3b_{x,y}/\lambda$  for optical masks.  $b_{x,y}$  are the mask periods in  $x$ - and  $y$ -direction and  $\lambda$  is the illumination wavelength. In Figure 1 left only the absorber layers 84 and 85 consist of two different materials (the respective absorber material itself and vacuum as the material around the absorber). All other layers (substrate, Mo and Si layers) have only one material and are therefore negligible for the computation time. The overall order number  $M$  in Figure 1 left is three. In contrast to that a multilayer defect drastically changes the situation. In Figure 1 right the corresponding situation is shown. Based on a multilayer defect model [1, 6] the defect particle deforms the whole multilayer structure. This has two important effects for the simulation: First of all, a large number of layers has to be used in order to describe correctly the deformed multilayer structure. Typical numbers are in the range of 1500 to 3000 layers. Secondly, due to the deformation all layers consist of more than one material (a mix of Mo and Si in each layer) and contribute consequently to the simulation time. The factor  $A$  is now in the range of 1500 to 3000 (instead of two as in Figure 1 left) with the result of a strongly extended simulation time that is now typically in the range of several hours.

In the optical case (e.g. at 193 nm), the convergence is a basic problem of all electromagnetic field solvers based on modal methods like Waveguide because of the significant refractive index differences between the materials. However, several mathematical optimizations, implemented in our solver, reduce this problem effectively with the result of a very good convergence in this case [1]. In contrast to that the EUV case is uncritical because the refractive indices of all materials are close to 1.

## 2.2. Data base extension of the Waveguide approach

As shown in the previous section, the computation time of a defective EUV multilayer is a very critical point and limits the application of the fully rigorous model to a relatively small number of individual computations. More comprehensive investigations like the simulation of a defect repair are more or less impossible. However, due to the high sensitivity of the simulation results on the defect parameters, the large defect parameter range, the complex structure of defective multilayers and the required accuracy the application of a fully rigorous EMF solver seems to be indispensable. Figure 2 illustrates the idea of the data base approach as a powerful solution of this problem.

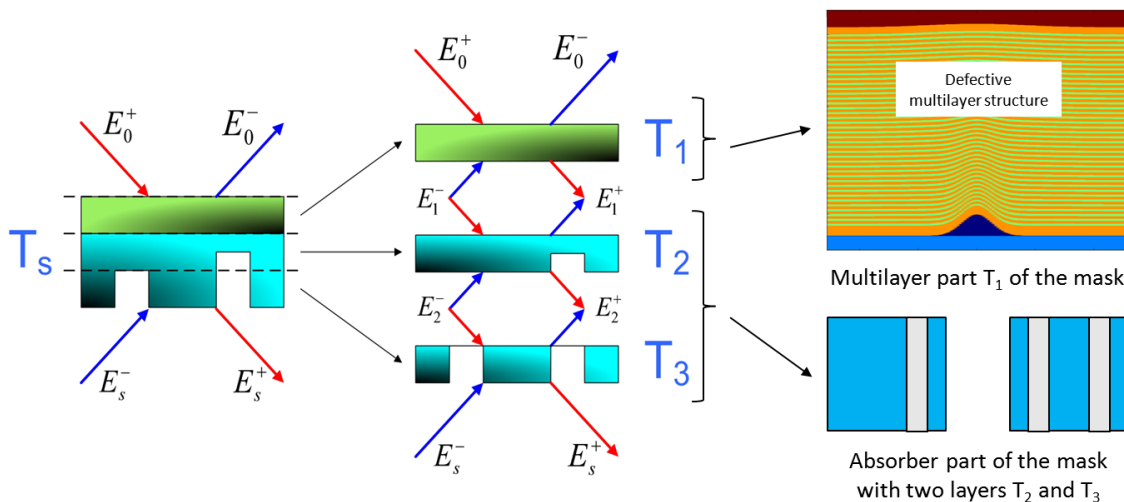


Figure 2: Basic idea of the data base approach: The mask to be simulated (left picture) is split up into several independent mask parts represented by their transfer matrices  $T_1$ ,  $T_2$ ,  $T_3$  (middle picture). The defective multilayer part ( $T_1$ ) is simulated “off line” with Waveguide and stored in a data base. The absorber parts ( $T_2$ ,  $T_3$ ) are computed “on demand” with Waveguide during an investigation and recombined with the defective multilayer part ( $T_1$ ) from the data base. The resulting transfer matrix is the same as  $T_s$  and is used for the spectrum computation.

The data base extension of our Waveguide solver provides two different operation modes. The “Data Base Mode” for the computation and storage of individual data base entries and the “Application mode” for the combination of data base entries with “on demand” computations. Using the example of a patterned EUV mask with a multilayer defect both modes are explained in the following.

### 2.2.1 “Data Base Mode” of the Waveguide solver

The multilayer defect is characterized by a set of parameters defining the defect particle geometry and the geometry of the multilayer’s top level layer. A specific defect model computes the propagation of the defect caused deformation through the multilayer from bottom to top [1, 6]. The result is a sampled three-dimensional structure of the deformed multilayer serving as input for the following diffraction spectrum computation. During this fully rigorous computation the transfer matrices of all the individual layers (Figure 1 right, typically 1500 – 3000 layers) are internally extracted and incrementally combined to the final overall transfer matrix characterizing the whole defective multilayer. Finally this overall transfer matrix is stored in a data base. By varying the defect parameters the “Data Base Mode” of the Waveguide solver can be used to fill up the defect data base independently and continuously. It should be mentioned again that the computation time of one defect simulation is relatively long (typically in the range of several hours) but the fully rigorous approach guarantees the highest possible accuracy. Of course, the “Data Base Mode” cannot only be used for defective EUV multilayers but also for the computation and storage of any mask structure or part of a mask structure. Moreover, different solvers like FDTD or analytical models can be combined with Waveguide enabling hybrid simulations.

### 2.2.2 “Application Mode” of the Waveguide solver

This operation mode is used during an investigation for the fast and fully rigorous simulation of patterned EUV masks with multilayer defects. In the first step the mask to be computed is split up into the defective multilayer part and into the absorber part ( $T_1$ ,  $T_2$ ,  $T_3$  in Figure 2). The defective multilayer part ( $T_1$  in Figure 2) is ignored assuming that the corresponding transfer matrix exists in the data base. If this is not the case one can either perform the multilayer computation or select a similar defect being available in the data base. In the next step the fully rigorous diffraction spectrum computation of the absorber part ( $T_2$ ,  $T_3$  in Figure 2) is performed. During this computation the transfer matrices of all absorber layers are internally extracted and combined to the overall transfer matrix of the whole absorber part. The computation time of this step is typically in the range of seconds up to minutes and can be performed “on demand” during an investigation. This enables the flexibility e.g. required for the investigation of a defect repair. In the following step the corresponding transfer matrix of the defective multilayer part is read from the data base and combined with the absorber part to the system transfer matrix ( $T_S$  in Figure 2). Finally, using  $T_S$  and the illumination spectrum the resulting reflected and transmitted mask diffraction spectra are computed (Figure 1 left). The computation time of the steps data-base-reading, transfer-matrix-combination and diffraction-spectrum-computation is relatively short and typically in the range of seconds. The result is a fully rigorous simulation of a patterned EUV mask with multilayer defect in a typical time range of seconds up to a few minutes. It has to be mentioned that there is one limitation in the current version of our Waveguide solver. At the moment it is not possible to combine mask parts with different pitches. The development of this feature is in progress and will be presented soon. However, the combination of mask parts computed with different numbers of diffraction orders is already possible.

### 2.2.3 Data base geometry effect

The split up and later recombination of a mask causes one specific geometry effect that has to be taken into account in all computations. Figure 3 demonstrates the situation. In the left picture the mask to be simulated is shown. In contrast to that in the right picture the actually computed mask structure can be seen. In case of a bump defect with an elevation on top of the multilayer (denoted by A in Figure 3) the splitting and later recombination of the mask causes the following geometry difference: Compared to the original mask, the absorber part is shifted at distance A. This distance is required to achieve homogeneous materials at the lower part of the absorber and at the upper part of the defective multilayer respectively. Except for a few extreme cases, investigations have shown (see the following Section 3) that a reduction of the absorber height according to the multilayer top elevation (denoted by B in Figure 3) is sufficient for an acceptable agreement with reference simulations using the correct mask geometry as shown in Figure 3 left. For the investigations a maximum top elevation of 5 nm was taken into account.

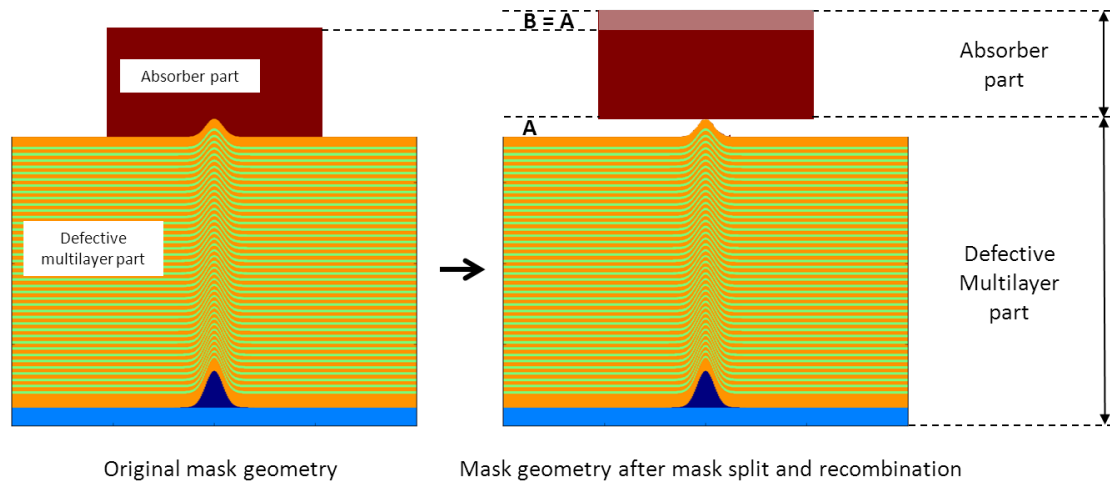


Figure 3: Defective EUV mask with absorber pattern to be simulated (left picture). The split up of the mask into the absorber part and defective multilayer part and the later recombination causes an absorber shift  $A$  with respect to the original mask (right picture). Except for a few extreme cases, investigations up to a maximum  $A$  of 5 nm have shown that a corresponding absorber height reduction of  $B$  compensates the shift sufficiently.

In case of a bump defect with no elevation on top of multilayer and in case of a pit defect with and without a depression on top of the multilayer the described geometry effect shows only a very small impact on the result and can be neglected. No specific compensation has to be done.

### 2.2.4 Numerical accuracy

Beside the geometry effect there are two more sources for potential differences between the data base approach and a standard simulation without using a data base. The generation of the data base and of the “on demand” computed mask parts (see previous Sections 2.2.1 and 2.2.2) is based on transfer matrices. All transfer matrices are extracted internally from intermediate results during a Waveguide computation. Therefore, in contrast to a standard simulation several additional mathematical operations with additional potential numerical imprecisions have to be performed. Secondly, the storage and reading of the computation results in/from a data base has a limited accuracy. However, the impact of both error sources is very small and negligible as shown in the following Section 3.

## 3. SIMULATIONS

In this section the accuracy and the speed of the data base approach with respect to corresponding simulations performed in the standard way without using a data base are investigated. Furthermore a defect repair simulation demonstrates the efficiency and functionality of the new data base approach. In the following “standard-simulation” denotes a computation performed without using any data base. The whole mask (absorber and defective multilayer) is simulated rigorously in one step using our Waveguide solver. This simulation guarantees the highest possible accuracy and serves as reference. “Data-base-simulation” denotes a simulation using the new data base approach as described above. The absorber part is computed rigorously “on demand” with Waveguide and the defective multilayer part is taken from a data base. Both parts are combined to the final result (details are given in Section 2.2.2). All defective multilayers of the data base are computed rigorously in advance with Waveguide too (details are given in Section 2.2.1). The speed advantage of data-base-simulations is obvious and will be demonstrated. Additionally, due to the effects described in Section 2.2.3 and 2.2.4 the investigation of the accuracy is very important and will be demonstrated too.

### 3.1 Simulation settings

All investigations are based on aerial images using the mask diffraction spectra from standard-simulations and from data-base-simulations. The following settings are used:  $\lambda = 13.5$  nm, conventional source,  $\sigma = 0.5$ , unpolarized,  $6^\circ$  chief ray

angel, NA = 0.35, 4x reduction. The mask consists of a standard multilayer with 40 MoSi double layers. In order to get a complete picture of the quality of the new data base approach the following absorber features and multilayer defects are investigated: 22 nm dense lines, 22 nm semi dense lines with a ratio of 1:3 and 22 nm dense contacts, three different bump defects with small, medium and large sizes, three different pit defects with small, medium and large sizes and three different defect positions for each feature type. In all cases the mask pitch was 352 nm (mask scale). The comparison between data-base-simulations and standard-simulations with respect to aerial images, CDs, process windows and the simulation speed was performed for the combination of all absorber features, defects and defect positions. After the evaluation of the results it was no more required to investigate more isolated lines as the simulations have shown that the dense structures are the most critical for the accuracy of the data base approach. In the same way the investigations have shown that bump defects are more critical whereas pit defects are in general uncritical for the accuracy. Consequently, the contact features were only investigated for the dense case in combination with bump defects. The sizes of all defects and their positions are shown in the following Tables 1 and 2:

Table 1: Definition of the defect sizes. The defect particle and the top level layer of the multilayer are Gaussian shaped. The deformation between particle and top level layer is computed with a defect geometry propagation model [1, 6]. A positive height represents a bump defect. A negative height corresponds to a depression representing a pit defect. The pit defects are assumed to propagate 1:1 between top and bottom. FWHM denotes the full width half maximum.

	Defect height	Defect FWHM	Height of top level layer elevation	FWHM of top level layer elevation
Small bump	10 nm	10 nm	1 nm	50 nm
Medium bump	20 nm	20 nm	3 nm	70 nm
Large bump	30 nm	30 nm	5 nm	90 nm
Small pit	-2 nm	30 nm	-2 nm	30 nm
Medium pit	-3 nm	50 nm	-3 nm	50 nm
Large pit	-5 nm	70 nm	-5 nm	70 nm

Table 2: Definition of the defect positions.

Defect position	Description
1	Dense lines: The center of the defect is located under the center between two lines
2	Dense lines: The center of the defect is located under the edge of a line
3	Dense lines: The center of the defect is located under the center of a line
4	Semi dense lines: The center of the defect is located under the center of a line
5	Semi dense lines: The center of the defect is located under the edge of a line
6	Semi dense lines: The center of the defect is located 22 nm away from the edge of a line
7	Dense contacts: The center of the defect is located under the center of a contact
8	Dense contacts: The center of the defect is located under the edge of a contact
9	Dense contacts: The center of the defect is located under the center between two contacts

Finally the combination of a defective multilayer and absorber computed with different numbers of diffraction orders is shown exemplarily for dense lines with the small bump defect at position 1. This investigation represents the qualitative behavior of all cases.

### 3.2 Accuracy and speed of the new approach

The combination of all features, defect sizes and defect position leads to an overall number of 45 individual investigations. Figure 4 shows exemplarily the result of one investigation for the dense lines with the medium bump defect at position 1. The same investigations were performed for all other combinations and are summarized in Table 3. The upper left picture of Figure 4 shows the aerial image at best focus resulting from the standard-simulation. The two lines are located at 22 nm and 66 nm with a corresponding shift to the left caused by the illumination angle of 6° from the right. The medium bump defect is located at position 1 indicated by the semi-white circle. The decrease of the intensity between the lines in the vicinity of the defect can be seen clearly. Three CDs are measured at the indicated positions (Pos. 1, Pos. 2 and Pos. 3 in Figure 4 upper left). The corresponding values can be found above the picture. For

the CD measurement a threshold to size for the defect free multilayer and 22 nm target was used. The upper center picture shows corresponding simulation results with the data-base-simulation. Finally the upper right picture shows the image and CD differences between the standard-simulation and the data-base simulation. In the lower line six process windows computed at the same positions 1 to 3 (Pos. 1, Pos. 2 and Pos. 3 in Figure 4 upper left) are shown. The black curves show the standard-simulations, the red curves the data-base-simulations. Since the process windows directly above the defect are relatively poor the y-coordinate of the positions was shifted some nanometers away from the center of the defect at 61 nm (see indicated positions in the upper left picture of Figure 4) but still being in the area of influence of the defect. For the other features corresponding CDs and process windows as close as possible to the defect were computed in the same way. The required shift depending on the feature type, defect size and position was adapted individually to all performed simulation. As a quality indicator for the identity of the process windows (identity between black and red curves) the overall window overlap OV is used. The corresponding value can be found above the respective picture. 100% denotes two identical process windows whereas 0% corresponds to completely different windows with no overlap.

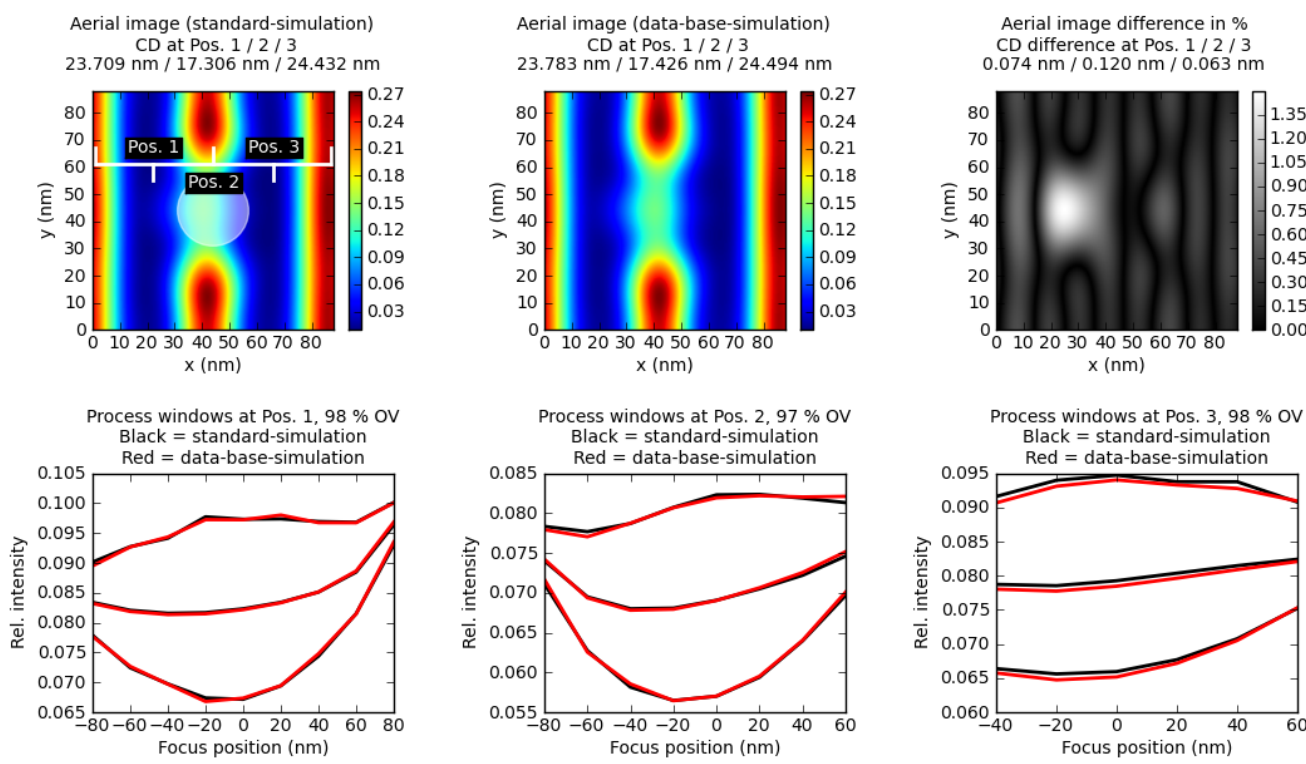


Figure 4: Comparison of a standard-simulation with a data-base simulation for dense lines with the medium bump defect at position 1.

In the example of Figure 4 the small difference of the images and the good agreement of the CDs and process windows of a standard-simulation and a data-base-simulation can be seen. The simulation time of the standard-simulation was 9500 seconds. Assuming that the defect is available in the data base and only the absorber is computed during the investigation the data-base-simulation takes only 20 seconds. All times are for a standard PC with a single 2.8 GHz CPU. In order to demonstrate that the small differences are almost completely coming from the data base geometry effect (see Section 2.2.3) and only a very small part is coming from the numerical imprecisions (see Section 2.2.4) Figure 5 shows the same investigation as in Figure 4 with one difference: The bottom of the absorber part in the standard-simulation (see Figure 3 left) is replaced by an vacuum layer with a thickness of  $\lambda$  in order to get the same geometry as for the data-base simulation (see Figure 3 right).

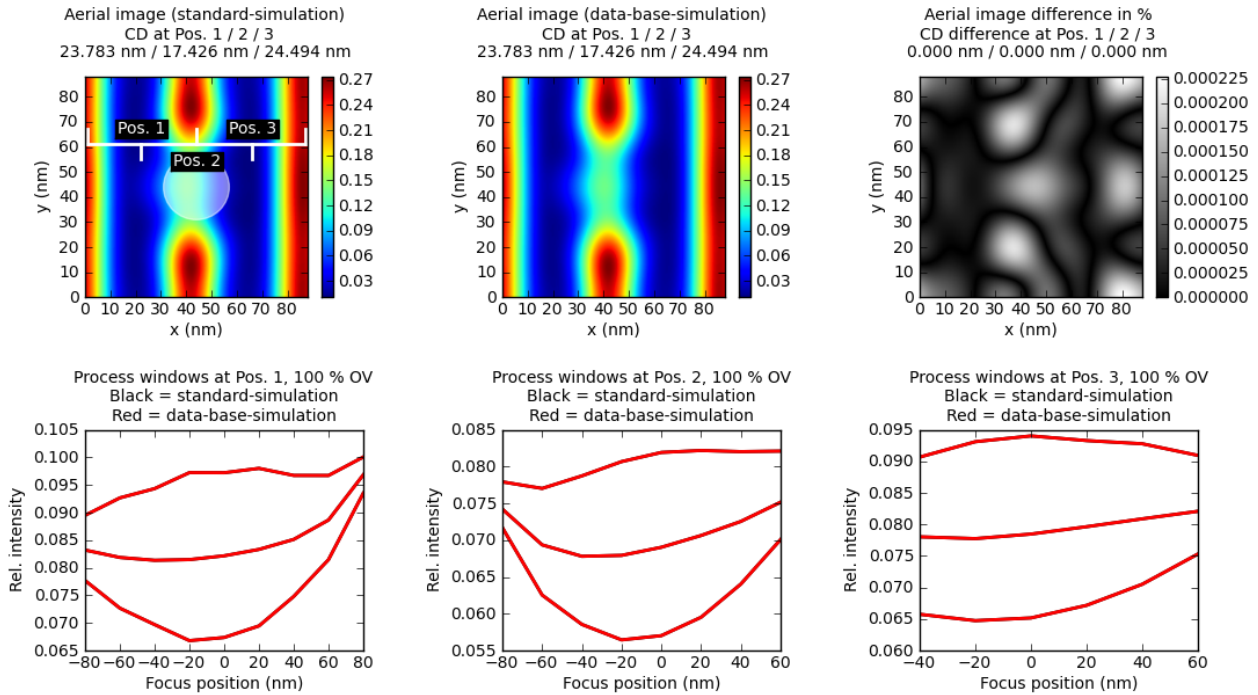


Figure 5: Same investigation as in Figure 4 with one difference: In order to get the same geometry as in the data-base-simulation the absorber in the standard-simulation is modified accordingly (see Section 2.2.3).

The nearly perfect agreement with a very small difference in the images only caused by numerical imprecisions (see Section 2.2.4) can be seen. In the same way as shown exemplarily in Figure 4 and 5 all other combinations are investigated. The results are summarized in the following Table 3:

Table 3: Simulation results for all investigated combinations. The defects and defect positions are defined in the Tables 1 and 2. The numbers in the columns 5, 6 and 7 correspond to the numbers shown in Figure 4 and described in the text. The numbers marked with \* in the lines 40 – 45 are computed with adapted intensities of the data-base-simulations in order to compensate the data base geometry effect (see text below the table and Section 2.2.3). All simulation times are for a standard PC with a single 2.8 GHz CPU.

		Absorber, all features are 22 nm	Defect	Defect position	Maximum image difference in percent	CD difference in nm of all measured CDs	Process window overlap in percent of all computed process windows	Simulation time in seconds of standard-simulation / data-base-simulation
1	Dense lines		Small bump	1	0.27	0.067 / 0.07 / 0.052	98 / 99 / 99	6300 / 20
2	Dense lines		Small bump	2	0.32	0.045 / 0.013	100 / 100	6300 / 20
3	Dense lines		Small bump	3	0.36	0.047 / 0.009 / 0.009	100 / 98 / 100	6300 / 20
4	Dense lines		Medium bump	1	1.35	0.074 / 0.12 / 0.063	98 / 97 / 98	9500 / 20
5	Dense lines		Medium bump	2	0.54	0.023 / 0.028	97	9500 / 20
6	Dense lines		Medium bump	3	0.9	0.017 / 0.071 / 0.005	98 / 92 / 98	9500 / 20
7	Dense lines		Large bump	1	2.25	0.042 / 0.0 / 0.113	96 / 96 / 95	12700 / 20

8	Dense lines	Large bump	2	1.2	0.078 / 0.085	96 / 97	12700 / 20
9	Dense lines	Large bump	3	1.2	0.029 / 0.156 / 0.045	95	12700 / 20
10	Semi dense lines 1:2	Small bump	4	0.16	0.048	99	6300 / 20
11	Semi dense lines 1:2	Small bump	5	0.16	0.077	98	6300 / 20
12	Semi dense lines 1:2	Small bump	6	0.16	0.093	98	6300 / 20
13	Semi dense lines 1:2	Medium bump	4	0.4	0.006	99	9500 / 20
14	Semi dense lines 1:2	Medium bump	5	0.36	0.114	95	9500 / 20
15	Semi dense lines 1:2	Medium bump	6	0.4	0.067	97	9500 / 20
16	Semi dense lines 1:2	Large bump	4	0.45	0.032	99	12700 / 20
17	Semi dense lines 1:2	Large bump	5	0.4	0.11	96	12700 / 20
18	Semi dense lines 1:2	Large bump	6	0.45	0.03	98	12700 / 20
19	Dense lines	Small pit	1	0.056	0.007 / 0.003 / 0.002	100 / 100 / 100	6200 / 20
20	Dense lines	Small pit	2	0.064	0.005 / 0.006	99 / 99	6200 / 20
21	Dense lines	Small pit	3	0.18	0.018 / 0.027 / 0.01	100 / 98 / 100	6200 / 20
22	Dense lines	Medium pit	1	0.105	0.007 / 0.001 / 0.001	100 / 100 / 100	9400 / 20
23	Dense lines	Medium pit	2	0.36	0.037 / 0.042	98 / 99	9400 / 20
24	Dense lines	Medium pit	3	0.4	0.033 / 0.047 / 0.005	99 / 97 / 99	9400 / 20
25	Dense lines	Large pit	1	0.28	0.007 / 0.005 / 0.009	100 / 100 / 100	12600 / 20
26	Dense lines	Large pit	2	0.72	0.129 / 0.021	98 / 100	12600 / 20
27	Dense lines	Large pit	3	1.05	0.045 / 0.182 / 0.162	97 / 93	12600 / 20
28	Semi dense lines 1:2	Small pit	4	0.072	0.056	99	6200 / 20
29	Semi dense lines 1:2	Small pit	5	0.045	0.025	100	6200 / 20
30	Semi dense lines 1:2	Small pit	6	0.04	0.022	100	6200 / 20
31	Semi dense lines 1:2	Medium pit	4	0.16	0.089	97	9400 / 20
32	Semi dense lines 1:2	Medium pit	5	0.12	0.092	99	9400 / 20
33	Semi dense lines 1:2	Medium pit	6	0.04	0.012	100	9400 / 20
34	Semi dense lines 1:2	Large pit	4	0.32	0.131	95	12600 / 20
35	Semi dense lines 1:2	Large pit	5	0.45	0.088	97	12600 / 20
36	Semi dense lines 1:2	Large pit	6	0.036	0.009	100	12600 / 20
37	Dense contacts	Small bump	7	1.2	0.008 / 0.013 / 0.002	97 / 96 / 97	6300 / 20
38	Dense contacts	Small bump	8	1.2	0.015 / 0.026	98 / 96	6300 / 20
39	Dense contacts	Small bump	9	1.2	0.02 / 0.122 / 0.01	96 / 94 / 96	6300 / 20
40	Dense contacts	Medium bump	7	3.2 2.7*	0.284 / 0.851 / 0.336 0.083*/0.306*/0.371*	90 / 80 / 90 93* / 80* / 91*	9500 / 20
41	Dense contacts	Medium bump	8	2.7 2.4*	0.539 / 0.344 0.25* / 0.344*	90 / 85 90* / 93*	9500 / 20
42	Dense contacts	Medium bump	9	3.2 2.7*	0.086 / 0.255 / 0.136 0.279*/0.011*/0.306*	90 / 80 / 90 93* / 95* / 93*	9500 / 20
43	Dense contacts	Large bump	7	4.0 3.0*	0.799 / 1.366 / 0.392 0.095* / 0.29* / 0.49*	80 / 60 / 80 90* / 90* / 90*	12700 / 20
44	Dense contacts	Large bump	8	2.7 2.7*	0.163 / 0.178 0.109* / 0.052*	90 / 92 92* / 95*	12700 / 20
45	Dense contacts	Large bump	9	3.6 2.7*	0.22 / 0.665 / 0.43 0.394*/0.011*/0.068*	91 / 75 / 85 90* / 90* / 90*	12700 / 20

If the absorber of the standard-simulation is adapted to the absorber of the data-base-simulation as described in Figure 5 all image differences and CD differences in Table 3 are almost zero and all process window overlaps are 100 %.

Regarding accuracy and speed of the data base approach the table shows the following results: In general data-base-simulations show a very good agreement with standard-simulations and can be used for all applications. The simulation time is 310 to 635 times faster (6200 s / 20 s – 12700 s / 20 s) enabling comprehensive investigations. Pit defects are in general uncritical providing an excellent agreement between data-base-simulations and standard-simulations. Depending on the size, bump defects are more critical and tends to result in larger but still uncritical differences compared to pits.

Dense features are more critical than less dense features and contacts are more critical than lines but all cases are still showing a good agreement between standard-simulations and data-base-simulations. Only in case of dense contacts with larger bump defects (lines 40 – 45 in Table 3) there are some differences compared to the standard-simulations. Depending on the application an additional compensation of the data base geometry effect (see Section 2.2.3) has to be applied. This is done in Table 3 for the mentioned cases (all corresponding numbers are marked with \*). The upper line of the respective case shows the results without any compensation. In the lower line the intensities of the data-base-simulations are reduced by the same percentage as the absorber height is reduced (see Section 2.2.3 and in Figure 3). After this intensity adaption an acceptable agreement with the standard-simulations can be observed too.

Finally, Table 4 shows exemplarily the combination of a defective multilayer (in all cases computed with 7 x 7 diffraction orders) with an absorber computed with different numbers of diffraction orders for the dense lines with the small bump defect at position 1. The same investigations as described before have been done. Since the multilayer defect is computed with 7 x 7 diffraction orders the absorber with the same number of orders serves as reference. The corresponding image and CD differences are zero and the process window overlaps are 100 % (see line 4 in Table 4). The selected example of Table 4 represents the qualitative behavior for all investigated cases.

Table 4: Combination of a multilayer defect computed with 7 x 7 diffraction orders with an absorber computed with different numbers of diffraction orders.

	Number of absorber diffraction orders	Maximum image difference in percent	CD difference in nm of all measured CDs	Process window overlap in percent of all computed process windows
1	4 x 4	22.5	2.545 / 2.693 / 2.515	25
2	5 x 5	20.0	2.395 / 2.724 / 2.827	25
3	6 x 6	5.4	0.209 / 0.122 / 0.336	80 / 89
4	7 x 7	0.0	0.0 / 0.0 / 0.0	100 / 100 / 100
5	8 x 8	4.5	0.177 / 0.333 / 0.424	83 / 91
6	9 x 9	4.5	0.1 / 0.354 / 0.47	86 / 88 / 89
7	10 x 10	4.5	0.3 / 0.24 / 0.21	87
8	11 x 11	4.5	0.34 / 0.27 / 0.23	86 / 86
9	12 x 12	4.5	0.32 / 0.23 / 0.2	88

The table clearly shows that the smallest order number of the mask parts to be combined determines the quality of the result. A lower order number of one part reduces the quality significantly (see Table 4 lines 1 - 3) whereas a higher number does not improve the result. This can be inferred from the fact that all numbers in the lines 5 – 9 of Table 4 do not change systematically with an increasing number of diffraction orders. They only show a certain error fluctuation in the same range.

### 3.3 Application example: Defect repair

Figure 6 shows schematically the application of the data base approach for the simulation of an EUV multilayer defect repair. On the left side the mask layout (22 nm dense lines with the medium bump defect at position 1) and the resulting aerial image is shown. A defect caused intensity loss in the bright area between the lines can be observed. The basic idea of a defect repair is to cut out the absorber around the defect in such a way that the additional intensity from the cut out area compensates the reduced reflectivity of the defect area as good as possible [7 - 9]. In Figure 6 a simple rectangular cut out geometry with vertical side walls and different sizes is shown. The impact on the aerial images can be seen clearly. However, for a better imaging performance more complex shapes have to be used [10]. The determination of a proper shape requires an optimization approach – also available in combination with our Waveguide solver – performing many individual simulations. This is only possible in an acceptable time frame with the presented data base approach. Depending on the shape complexity and the degrees of freedom, an optimization can require several hundreds of mask diffraction simulations. Assuming exemplarily 300 mask simulations this would take more than 30 days on a single 2.8 GHz CPU with the standard-simulations, whereas the data-base-simulations only need a few hours for the same task. One can see that the data base approach provides the only practicable opportunity to perform such an investigation with rigorously computed mask defects.

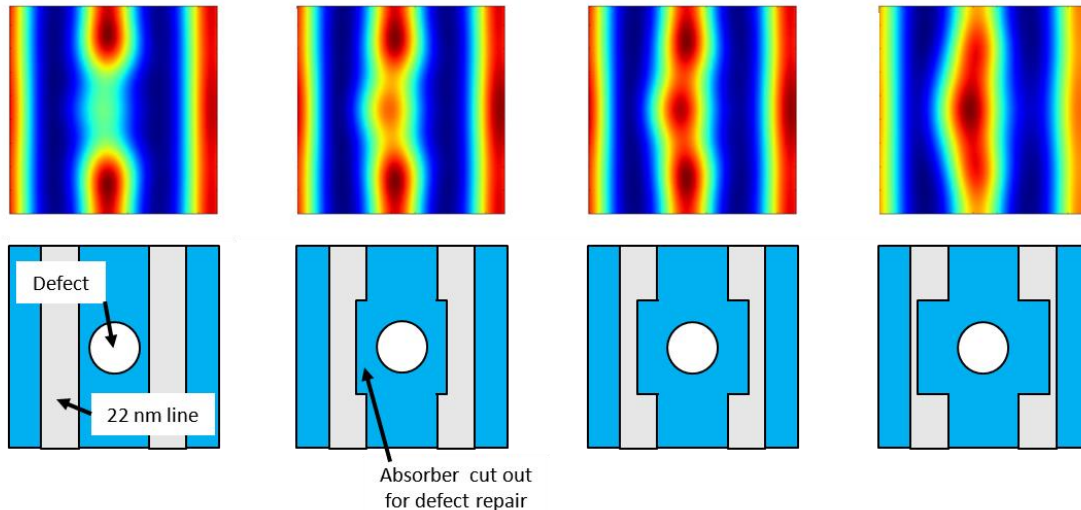


Figure 6: Schematic demonstration of the simulation of an EUV multilayer defect repair. Lower line: Mask layouts, upper line: Resulting aerial images. Left: Initial situation, mask with defect and without repair. Following rows from left to right: Different repair shapes with a smaller, medium and larger cut out area. The impact of the defect and of the repairs on the aerial images can be seen clearly. This example only demonstrates the basic idea of a defect repair. For a better imaging performance more complex shapes resulting from an optimization loop with many individual simulations have to be used [10].

#### 4. CONCLUSION

This paper presents the extension of the well-established rigorous EMF solver Waveguide with a defect data base for the fast and fully rigorous simulation of patterned EUV masks with multilayer defects. The very good agreement between standard-simulations (without using any data base) and the new data base approach is shown. Only a few extreme cases of dense contacts with large bump defects need an additional correction in order to have the same good agreement with the standard-simulations. Assuming that a selected defect is available in the data base the time advantage of the new approach is significant. Typical simulation times are in the range of seconds up to a few minutes, whereas corresponding standard-simulations typically take several hours. Due to the very short simulation times the new data base approach provides the opportunity to perform comprehensive investigations like EUV multilayer defect repairs based on rigorously computed masks.

#### ACKNOWLEDGEMENT

The authors would like to thank the European Commission and the German BMBF for funding parts of this work in the framework of the European EXEPT project.

#### REFERENCES

- [1] Evanschitzky, P., Erdmann, A., "Fast near field simulation of optical and EUV masks using the waveguide method," Proc. SPIE 6533, (2007)
- [2] Taflove, A., "Computational electrodynamics: the Finite-Difference Time-Domain method," Artech House Publisher, (1995)
- [3] Lucas, K. D., Tanabe, H., Strojwas, A., "Efficient and rigorous three-dimensional model for optical lithography simulation," J. Opt. Soc. Am. A 13, p. 2187, (1996)

- [4] Moharam, M. G., Pommet, D. A., Grann, E. B., Gaylord, T. K., "Simple implementation of the rigorous coupled-wave analysis for surface relief gratings: Enhanced transmittance matrix approach," *J. Opt. Soc. Am. A* 12, p. 1077, (1995)
- [5] Turunen, J., "Form birefringence limits of Fourier expansion methods in grating theory: errata," *J. Opt. Soc. Am. A* 14, p. 2313, (1997)
- [6] Ito, M., Ogawa, T., Otaki, K., Nishiyama, I., Okazaki, S., Terasawa, T., "Simulation of multilayer defects in extreme ultraviolet masks," *Jpn. J. Appl. Phys. P.* 40, 2549-2553, (2001)
- [7] Ray-Chaudhuri, A. K., Cardinale, G., Fisher, a., Yan, P.-Y., Sweeney, D. W., "Method for compensation of extreme-ultraviolet multilayer defects," *J. Vac. Sci. Technol. B* 17, p. 3024, (1999)
- [8] Jonckheere, R., Bret, T., den Heuvel, D. V., Magana, J., Gao, W., Waiblinger, M., "Repair of natural EUV reticle defects," *Proc. SPIE* 8166, (2011)
- [9] Bret, T., Jonckheere, R., den Heuvel, D. V., Baur, C., Waiblinger, M., Baralia, G., "Closing the gap for EUV mask repair," *Proc. SPIE* 8171, (2012)
- [10] To be presented at SPIE Advanced Lithography, (2013)